Journal of The Electrochemical Society

The Electrochemical Society
Advancing solid state & electrochemical science & technology

OPEN ACCESS

A Nanoscale Study of Thermally Grown Chromia on High-Cr Ferritic Steels and Associated Oxidation Mechanisms

Journal of The Electrochemical Society, 2020 **167** 061502

A Nanoscale Study of Thermally Grown Chromia on High-Cr Ferritic Steels and Associated Oxidation Mechanisms

Ashok Vayyala,[1] Ivan Povstugar,[1,z] Dmitry Naumenko,[2] Willem J. Quadakkers,[2] Heike Hattendorf,[3] and Joachim Mayer[4]

[1]*Central Institute for Engineering, Electronics and Analytics (ZEA-3), Forschungszentrum Jülich GmbH, Jülich, Germany*
[2]*Microstructure and Properties of Materials (IEK-2), Forschungszentrum Jülich GmbH, Jülich, Germany*
[3]*VDM Metals International GmbH, Altena, Germany*
[4]*Central Facility for Electron Microscopy (GFE), RWTH Aachen University, Aachen, Germany*

Fe-22Cr-0.5Mn based ferritic steels are used as interconnect materials for solid oxide fuel/electrolysis cells. Four steel samples, including the commercial steel Crofer 22 H, were oxidized at 800 °C in a model Ar-4%H_2−4%H_2O atmosphere simulating the fuel side of the cells and investigated by atom probe tomography (APT) in conjunction with electron microscopy and thermogravimetry. All steels form an oxide scale mainly consisting of $MnCr_2O_4$ spinel on top of Cr_2O_3. APT revealed segregation of minor alloying constituents (Nb and Ti) to chromia grain boundaries and highlighted their effect on mass transport through the chromia scale. Relationships between segregation activity of individual elements (in terms of Gibbsian interfacial excess), oxide scale microstructure and alloy oxidation rate have been established based on the APT results. Comparison of segregation activities revealed that vacancies formation due to Wagner-Hauffe doping with aliovalent Ti and Nb impurities cannot be solely responsible for faster oxidation, assuming alteration of the grain boundary structure and associated changes of their mass transport properties. Controlled Si addition to the alloy (about 0.4 at%) suppresses the detrimental effect of Nb on the oxidation resistance but results in formation of a thin, although still discontinuous, SiO_2 layer at the metal-oxide interface.
 [DOI: 10.1149/1945-7111/ab7d2e]

Manuscript submitted November 18, 2019; revised manuscript received March 4, 2020. Published March 19, 2020.

Supplementary material for this article is available online

Solid oxide fuel cells (SOFCs) have received a great deal of attention as an alternative to conventional power generation due to its high energy conversion efficiency and low greenhouse gas emissions.[1] A solid oxide electrolyzer cell (SOEC) is the reverse operation mode of a SOFC, which converts electric power to chemical fuel enabling long-term storage of the energy obtained from renewable sources.[2,3] An important component of both these cell types, the interconnect, serves to assemble individual cells into a functional device, provides electrical connection between them and, at the same time, separates different atmospheres present at the cathode (air in SOFC/fuel in SOEC) and anode (fuel in SOFC/air in SOEC) sides of the cell. Solid oxide cells currently operate at temperatures of about 800 °C, although significant efforts are being undertaken to further decrease the operating temperature.[4] The general demands to interconnect materials are good high-temperature strength, similarity of thermal expansion coefficients with the active cell elements, good electrical conductivity as well as high oxidation resistance in all relevant atmospheres to provide long operational lifetime.[5]

One of the most promising materials for interconnects are high-Cr ferritic steels due to their strength, resistance to brittle fracture compared to ceramic counterparts and formation of a thermally-grown Cr_2O_3 protective surface scale under high-temperature oxidation.[6,7] Cr_2O_3 has a reasonable electronic conductivity at high temperatures as compared to other typical protective scales, such as Al_2O_3 or SiO_2, which makes this steel class preferable for interconnects manufacturing.[8] However, when exposed to wet air, chromia may transform into volatile components, so it requires a barrier layer to prevent direct contact with the gas components.[9] This can be achieved e.g. by addition of Mn to the steel, which promotes formation of a Mn-containing spinel layer on the top of chromia.[10] High-Cr ferritic steels may also contain other alloying elements, either introduced intentionally to improve the microstructure and properties (e.g. strengthening with intermetallic phases, oxide-precipitation strengthening the vicinity of oxide-alloy interface, improvement of the oxide scale adherence etc.)[6] or remaining as technical impurities from the steel manufacturing process. These minor additives may enter the forming chromia/spinel scale under operation temperatures, or even form an additional oxide layer, thereby critically affecting the oxidation resistance or other alloy properties.[11] For example, residual Si used as a deoxidizer during alloy melting can form a thin electrically insulating SiO_2 layer at the alloy-oxide interface, which deteriorates current flow and disrupts the operation of a SOFC/SOEC device.[12] Therefore, careful alloy design and compositional tuning is required to achieve high interconnect performance, which requires understanding of the role of all alloy constituents, including minor additives, in the oxidation processes under operation conditions.

Extensive studies have been devoted to this topic in the recent decades.[13–17] Although numerous empirical rules about the influence of individual elements (and their interplay) on oxidation behavior have been derived so far,[17] there is still a lack of understanding of the underlying oxidation mechanisms. Characterization of thermally grown oxides at the nanoscale can retrieve the distribution of various elements and reveal the diffusion pathways, which are responsible for oxide scale formation and eventually for the oxidation resistance. Electron microscopy based methods and especially transmission electron microscopy (TEM) are conventionally used for the microstructure characterization of oxides.[18–22] Alternatively, atom probe tomography (APT) has unique capabilities to reveal minor elements presence and their segregation to grain boundaries (GBs) and interfaces, which can play the key role in mass transport through the oxide scale.[11,23,24] APT has been successfully employed in the recent years for studies of oxide scales thermally grown on steels[23–27] as well as on other alloy types.[28–33]

A family of high-Cr steels including Crofer 22 H suitable for operation as SOFC/SOEC interconnects has been developed in FZ Jülich and commercialized by VDM Metals.[34–37] Beyond the base elements (Fe, Cr and Mn) and processing impurities (Si and Al), the alloy contains additions of Nb and W promoting formation of the strengthening Laves phase,[7] Ti to form fine titania-base precipitates strengthening the sub-oxide region[12] and La to improve oxide scale adhesion.[38] The earlier studies revealed formation of a duplex-base

[z]E-mail: i.povstugar@fz-juelich.de

oxide scale consisting of $MnCr_2O_4$ spinel over the base Cr_2O_3 layer in these alloys,[39] and demonstrated a strong detrimental effect of Nb on the oxidation resistance of this steel class in H_2-H_2O containing atmospheres.[7,11] APT helped to reveal strong Nb segregation to chromia grain boundaries, which was assumed to result in formation of cationic vacancies due to Cr^{3+} substitution with higher charged Nb^{4+}/Nb^{5+} ions and associated diffusion enhancement along GBs. In the present work we employ APT for a more extended study of the Crofer 22 steel family, in particular, to reveal the role and interplay of Ti, Nb and Si in high-temperature (800 °C) oxidation processes in the Ar-4%H_2−4%H_2O atmosphere, modeling a fuel side of SOFC/SOEC cells. A focus in the present study has been made on the chromia layer, since it forms first under the given oxidation conditions,[39] so its microstructure controls the diffusion of oxygen and metallic ions during further oxidation stages. Another focus has been put to the analysis of the metal-oxide interface, which is critical for the oxide scale adherence as well as the electrical conductivity of an interconnect.[40,41]

Experimental

The commercial steel Crofer 22 H was selected as the base alloy, and its modifications were produced by removal of Nb, Ti or Si to study the effects of these additions. The steels were manufactured by VDM Metals by vacuum melting. An ingot of approximately 10 kg was cast and subsequently hot rolled down to sheets of 2 mm thickness. The actual chemical compositions of the steels were analyzed by inductively coupled plasma optical emission spectroscopy (ICP-OES) and are given in Table I. For reader's convenience the alloys were designated in the present paper following their minor elements content, where Nb, Ti and Si stand for additions of these elements. The alloys names given in the parenthesis refer to their designations in commercial use or in the lab as well as in our earlier publications.

Specimens of dimensions 20 × 10 × 2 mm for oxidation testing were machined from the hot rolled sheet by laser cutting. All machined samples were ground down to a 1200 grit surface finish with SiC abrasive papers. Prior to high temperature exposure, the specimens were ultrasonically cleaned with ethanol. Oxidation kinetics at 800 °C in Ar-4%H_2−4%H_2O test gas was measured by thermogravimetry using a Setaram TG 92 microbalance. Specimens were heated to the test temperature at a rate of 90 K min^{-1} in the test gas, kept at 800 °C for 72 h, and subsequently furnace cooled at approximately 10 K min^{-1}.

The microstructure of the oxidized samples was examined by scanning electron microscopy (SEM) using a Zeiss Supra 50VP instrument (Carl Zeiss Microscopy GmbH, Germany). For cross section SEM investigation, the specimens were mounted in an epoxy resin. Prior to mounting, the specimens were coated with an approximately 100 nm thick gold layer to create the electrically conductive surface, and subsequently electroplated with Ni using $NiSO_4$ solution. The Ni layer mechanically supports the oxide scale during further metallographic preparation, and additionally improves the contrast between the oxide scale and the mounting material during optical and electron microscopy observations.

TEM samples were prepared using a Zeiss Auriga cross beam focused ion beam (FIB) with a Ga ion source (Carl Zeiss Microscopy GmbH, Germany). High resolution electron imaging was carried out using a Zeiss Libra 200 transmission electron microscope (Carl Zeiss Microscopy GmbH, Germany) with accelerating voltage of 200 kV. Elemental analysis of the oxide scale was performed by energy dispersive X-ray spectroscopy (EDS) using a X-Max 80 detector (Oxford Instruments, UK).

For APT investigation of chromia scales and metal-oxide interfaces, specimens were prepared from the cross-sectional SEM samples by a conventional lift-out method[42] using a Helios Nanolab 650i dual beam FIB (Thermo Fisher Scientific, USA). APT specimens from the chromia scale were prepared perpendicular to the growth direction (parallel to the oxide scale surface) to maximize the number of grain boundaries in APT datasets, since chromia grains appeared textured in the growth direction. APT specimens containing the metal-oxide interface were prepared perpendicular (to

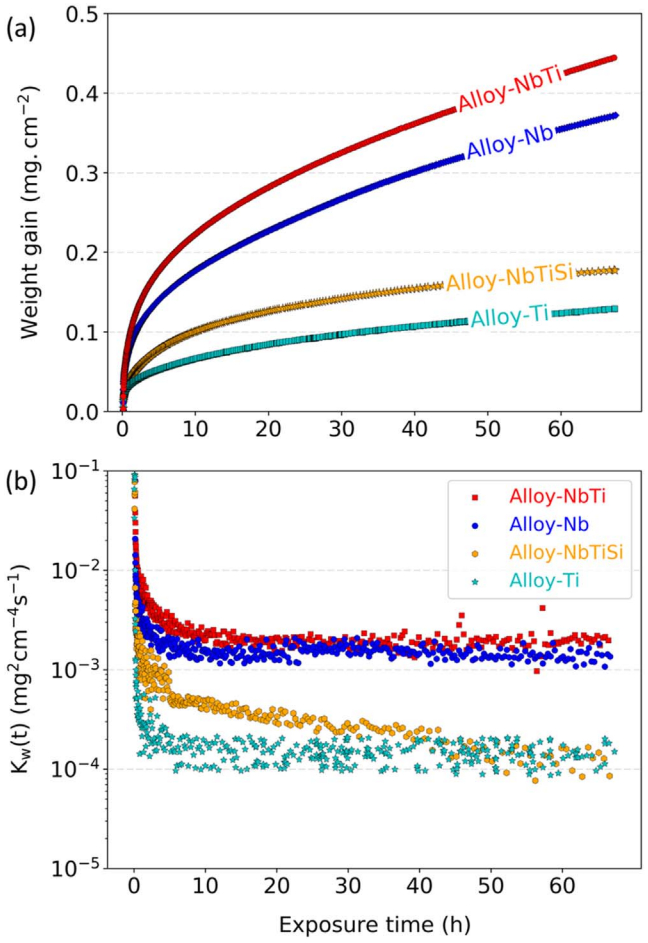

Figure 1. Thermogravimetric test results acquired during isothermal oxidation of four different alloys at 800 °C in Ar-4%H_2−4%H_2O: (a) mass change as a function of the exposure time and (b) instantaneous "apparent" parabolic rate constant $k_w(t)$ as a function of the exposure time. The error of the weight gain measurements is <1 μg cm^{-2}.

Table I. Chemical composition of the investigated alloys as determined by ICP-OES (in at %).[a] The alloys are designated based on the respective additions of Nb, Ti and Si. The respective commercial/lab names are mentioned in the parenthesis.

	Fe	Cr	Mn	Al	Si	Nb	Ti	La	W	C	N
Alloy-NbTiSi (Crofer 22 H)	73.31	24.64	0.44	0.04	0.42	0.31	0.08	0.03	0.3	0.03	0.06
Alloy-NbTi (KCL)	74.80	23.58	0.52	0.02	0.04	0.66	0.17	0.06	—	0.05	0.07
Alloy-Ti (Crofer 22 APU)	75.36	24	0.41	0.03	0.02	—	0.06	0.04	—	<0.01	0.01
Alloy-Nb (KCD)	74.48	24.22	0.47	0.02	0.04	0.63	—	—	—	0.02	0.08

a) Alloys additionally contain B and S in concentrations <0.01 at%.

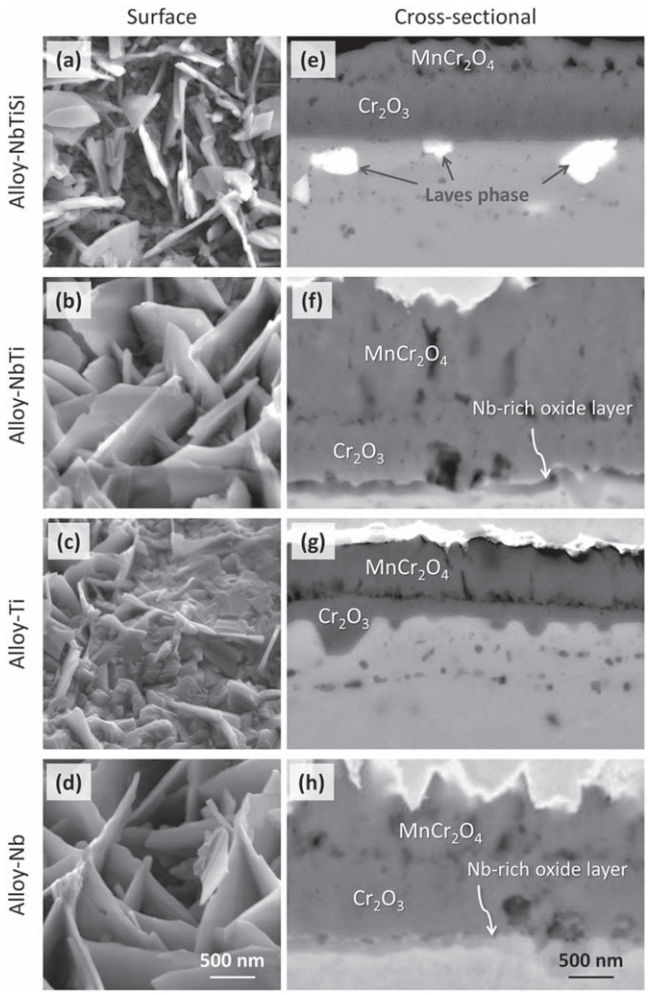

Figure 2. Surface morphologies (left column) and cross sectional (right column) SEM micrographs of the alloys exposed for 72 h at 800 °C in Ar-4%H_2−4%H_2O: (a) and (e) Alloy-NbTiSi, (b) and (f) Alloy-NbTi, (c) and (g) Alloy-Ti, (d) and (h) Alloy-Nb.

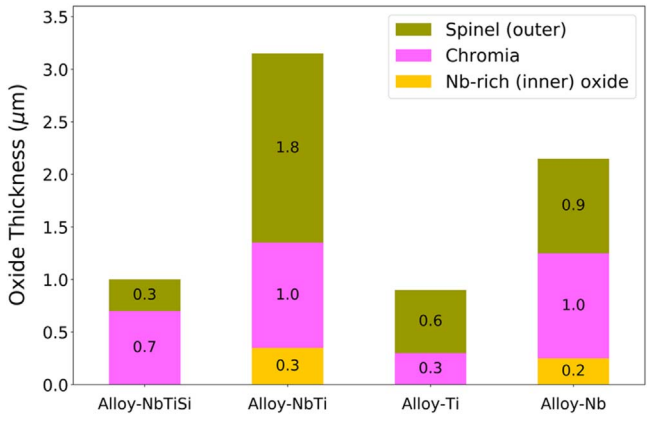

Figure 3. Thicknesses of the different layers in the oxide scale of the studied alloys determined from SEM image analysis.

maximize the analyzed interface area) as well as parallel (to minimize the influence of local magnification effect at the interface) to the growth direction. APT analysis was performed using a LEAP4000X HR instrument (Ametek Inc., USA) operating in laser mode with laser pulse frequencies of 200–250 kHz, laser pulse energies of 30–50 pJ and detection rate of 0.005 ions per pulse. The base specimen temperature was maintained at 50 K for all measurements. At least three datasets were measured for each alloy and region of interest. APT data reconstruction and analysis was carried out using the Integrated Visualization and Analysis Software (IVAS™) package 3.6.8 (Ametek Inc.). The details of the reconstruction procedure are given in the Supplementary Information. (available online at stacks.iop.org/JES/167/061502/mmedia).

Results

Oxidation kinetics.—Figure 1a shows the thermogravimetric data obtained during isothermal oxidation of the alloys at 800 °C in Ar-4%H_2−4%H_2O. All studied alloys exhibited weight gain from the very beginning (transient oxidation stage). The base Alloy-NbTiSi showed a maximal specific weight gain approximately equal to 0.18 mg·cm^{-2}. When Alloy-Ti (i.e. the variant without Nb and Si) was exposed, the maximal weight gain slightly reduced to 0.13 mg·cm^{-2}, while for both Alloy-Nb and Alloy-NbTi (note excess Nb content compared to Alloy-NbTiSi) the weight gain increased significantly.

Figure 1b shows the instantaneous "apparent" parabolic rate constants $k_w(t)$ calculated from the mass change data plotted in Fig. 1a. The procedure for the calculation was described elsewhere.[43] After an initial transient period of about 10 h, the rate constants become virtually time independent, except the base Alloy-NbTiSi, indicating an approximate parabolic time dependence of the oxide scale thickness. This would be expected from the classical oxidation theory, if transport processes through the oxide are rate determining:

$$(\Delta m)^2 = k_w \cdot t \qquad [1]$$

where Δm is the area specific weight gain (mg·cm^{-2}) and t is the exposure time (h).

It should be noted that only one sample for each alloy was tested in the thermogravimetric measurements. However, as the specimen surface preparation and the test procedures were identical for all alloys, and the SEM cross-section analysis revealed very uniform morphologies and compositions of the oxide scales, only small discrepancies in the weight gain curves (compared to the differences between the alloys) could be expected in replicated measurements.

Electron microscopy analysis.—Figure 2 depicts the surface morphologies and cross sections of the studied alloys as imaged by SEM. The oxides show a plate-like morphology with well-developed plates for Alloy-NbTi (Fig. 2b) and Alloy-Nb (Fig. 2d), whereas this morphology just started to develop on the surface of Alloy-Ti (Fig. 2c).

The cross-sectional SEM images show an oxide scale consisting of the outermost $MnCr_2O_4$ spinel and the inner chromia layers (see the earlier work for structural identification[11]). Two Nb-containing alloys (Alloy-Nb and Alloy-NbTi) show an additional layer of 100–200 nm thickness between the chromia layer and the metal matrix. All Ti-containing alloys exhibit an internal precipitation zone underneath the oxide scale. Additionally to the oxide phases, bright regions in Alloy-NbTiSi show the presence of a Laves phase of the Fe_2Nb-base stoichiometry.

The average thicknesses of the different oxide subscales derived from SEM image analysis are presented in Fig. 3. It can be concluded that the overall thickness increases after Nb addition to the alloy, correlating with the thermogravimetric data and indicating a decrease in oxidation resistance. Comparison of Alloy-Nb and Alloy-NbTi reveals a qualitatively similar effect of Ti. Si addition to the alloy greatly mitigates the detrimental Nb influence and eliminates the formation of the additional inner layer between Cr_2O_3 and the alloy matrix.

More detailed information on the oxide structure formed in the Ar–H_2–H_2O atmosphere was retrieved by TEM analysis in the scanning mode (STEM) in conjunction with EDS mapping. The results for Alloy-NbTiSi, which contains all studied minor additives,

are presented in Fig. 4a. Although a duplex spinel/chromia surface scale with fine-grained structure can be distinguished, EDS maps also reveal the presence of spinel grains deeply penetrating into the Cr_2O_3 layer. Additionally, a thin Si- and Nb-rich layer was found by EDS at the alloy-oxide interface, which was not recognizable in SEM due to either its lower resolution or a small step formed on the polished SEM cross-sectional sample around the metal-oxide interface. The region beneath the oxide scale contains numerous TiO_2 precipitates and a few Laves phase inclusions rich in Nb, Si and W.

The duplex scale structure was observed by STEM for all other studied alloys, although with a smaller amount of internal spinel inclusions compared to the Alloy-NbTiSi. An example of the Ti-free Alloy-Nb is presented in Fig. 4b, which additionally shows no internal precipitation but a thick Nb-rich oxide subscale. Besides, segregation of Nb at chromia grain boundaries is distinguishable in the corresponding EDS map.

Unfortunately, STEM is not capable to provide reliable information about chemistry of the grain boundaries and phase interfaces at low segregation levels, as well as to accurately quantify and compare the segregation activity of different elements in different alloys. Since GBs and interfaces often serve as fast diffusion path and provide accelerated mass transport through the oxide scale, this information can be crucial for understanding the oxidation mechanisms. To address these issues, further investigations were performed using atom probe tomography, which provides a higher level of elemental detection sensitivity.

APT analysis of the chromia scale.—STEM-EDS demonstrates an apparently uniform GB segregation pattern in the chromia scale (see e.g. Nb map in Fig. 4b) for all alloys. Nevertheless, variations of segregation behavior across oxide scales can take place.[24,44] In order to ensure a correct comparison between the alloys, all APT specimens from the chromia scales were taken from their middle part.

Figure 5a shows APT elemental maps of key impurities detected in the Cr_2O_3 scale on the Alloy-NbTiSi. Mn shows a clear tendency to segregate at chromia GBs and is also present in local Mn-rich regions with compositions matching $MnCr_2O_4$ spinel, i.e. it forms inner spinel inclusions in the chromia layer. Figs. 5b and 5c shows averaged elemental concentration profiles across chromia GBs and proximity histograms[45] across chromia/spinel interfaces, respectively. Ti and especially Nb segregate to grain boundaries at substantially lower levels compared to Mn. Si exhibits a weak tendency to GB segregation and additionally enters in marginal amounts the inner spinel precipitates. Al appears as a solute in chromia grains without a pronounced tendency to segregate at GBs.

Table II summarizes the bulk composition of the chromia phase in all studied alloys, including both grains and grain boundaries. All measurements show oxygen deficiency of 2–4 at% as compared to the nominal Cr_2O_3 stoichiometry. Such a deficiency is often observed in APT analysis of many oxide materials and originates from artifacts of the field evaporation process, i.e. not related to any true non-stoichiometry of the oxide phase.[46,47] Despite pronounced GB segregation, the total amount of impurities in chromia does not exceed 0.1 at% for each element, except Ti, in all alloys.

Figure 6a shows the elemental distribution within the chromia scale as analyzed by APT for Alloy-NbTi (Si-lean version of the base alloy), which demonstrates the highest oxidation rate. Elemental segregation of Ti, Mn and Nb at chromia grain boundaries was detected in this alloy as well. The quantitative analysis reveals however substantial differences with respect to the base alloy: GBs accumulate large levels of Ti and Nb, while the Mn peak concentration remains at a similar level (see Fig. 6b). Beside GB segregation, Ti also dissolves in chromia grains with concentrations up to 0.8 at%, thereby increasing the total amount of Ti in the chromia scale almost tenfold as compared to that of the base alloy. At the same time, no inner spinel inclusions were found in Alloy-

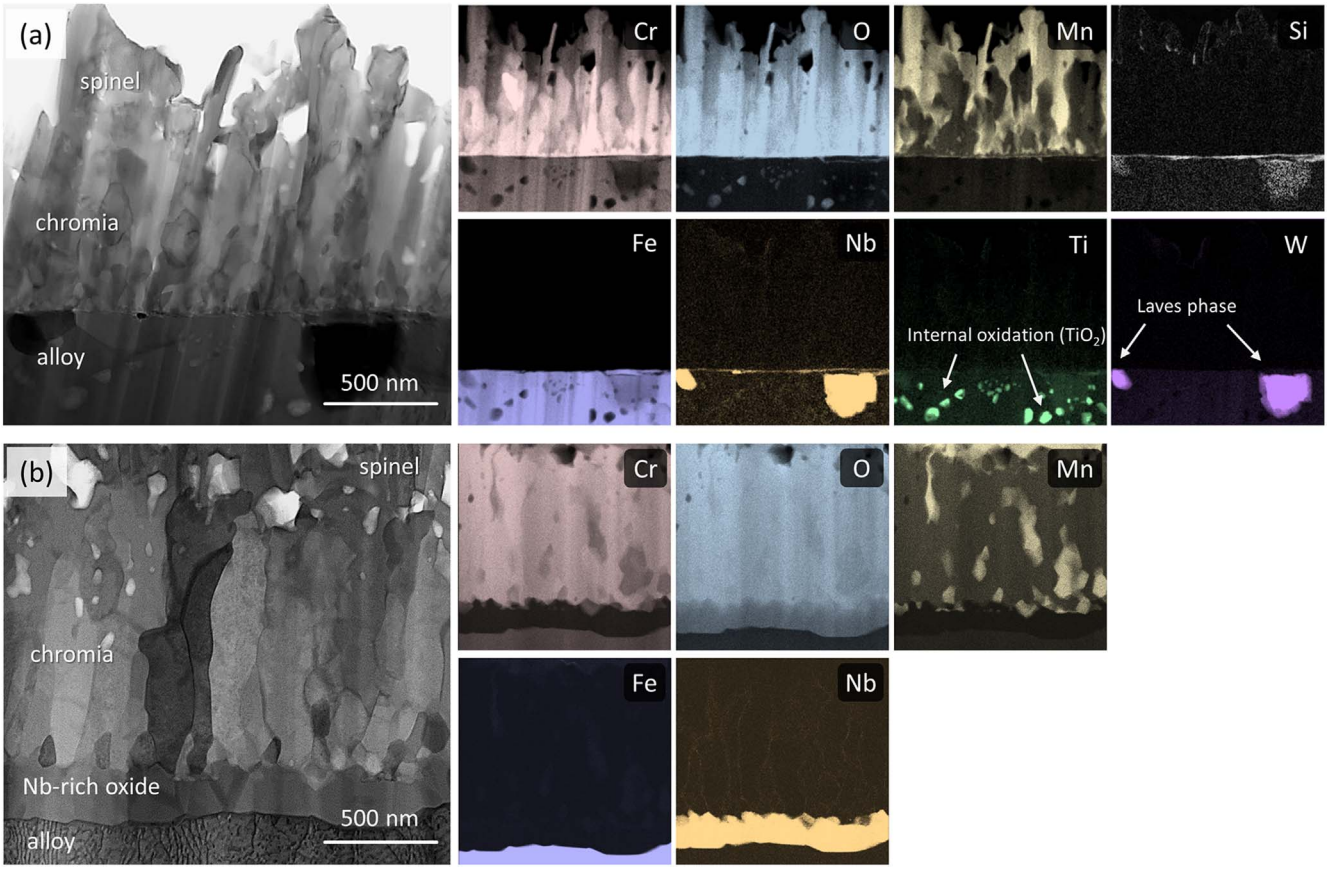

Figure 4. Bright-field STEM images and corresponding EDS elemental maps of (a) base Alloy-NbTiSi and (b) Alloy-Nb oxidized for 72 h at 800 °C in Ar-4%H_2−4%H_2O.

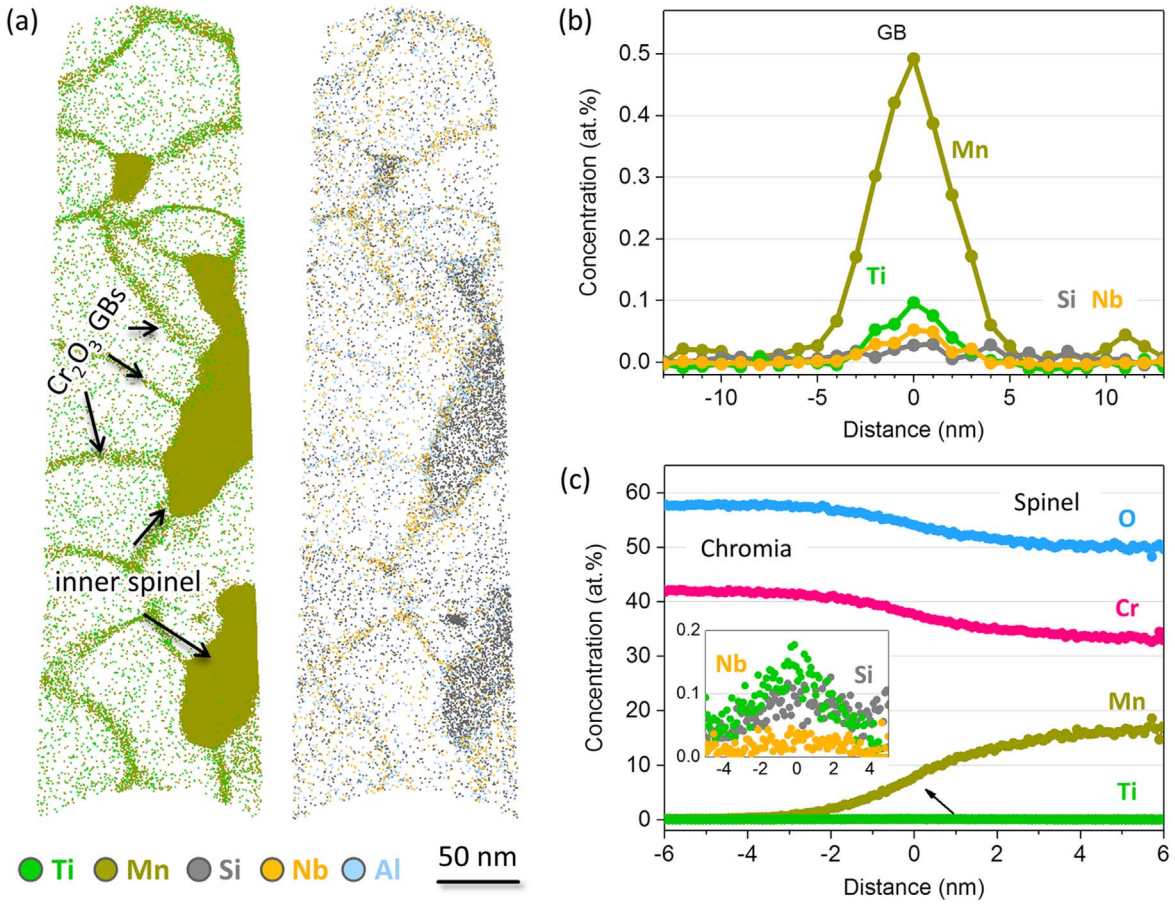

Figure 5. APT analysis of the Cr_2O_3 scale thermally grown on Alloy-NbTiSi (base alloy) after 72 h oxidation at 800 °C in Ar-4%H_2−4%H_2O: (a) atom maps of Ti, Mn, Si, Nb and Al; (b) elemental concentration profiles across GBs in the chromia scale; (c) proximity histograms across an interface between chromia and inner spinel grains. The inset shows a magnified view at the same interface to highlight minor impurities.

Table II. Bulk compositions (in at%) of the chromia scale retrieved from the APT analysis. Both grain interiors and grain boundaries were included into the analyzed volumes.

	O	Cr	Mn	Si	Ti	Nb	Al
Alloy-NbTiSi (base)	57.8	42.0	0.07	0.02	0.09	0.004	0.004
Alloy-NbTi	56.2	41.9	0.06	0.09	0.8	0.10	0.06
Alloy-Ti	56.3	42.7	0.10	0.01	0.7	—	0.04
Alloy-Nb	58.7	41.0	0.06	—	—	0.10	0.001

NbTi. Residual Si was found in chromia predominantly as SiO_2 inclusions sparsely localized at grain boundaries. More details of the APT analysis of this alloy can be found in the previous work.[11]

The oxide scale formed on Alloy-Ti and Alloy-Nb shows segregation behavior for Ti and Nb at chromia grain boundaries similar to that observed for Alloy-TiNb. Elemental concentration profiles built across GBs (Fig. 7) show substantial enrichments for these elements. Mn segregation shows slightly different trends: while the Mn peak concentration at chromia GBs reaches nearly 0.6 at% for Alloy-Ti (being close to that in the base alloy), it remains twice lower for Alloy-Nb.

The primary alloying element (Fe) was not detected by APT in the chromia scale of all studied alloys. Aluminum was detected predominantly as a non-homogeneous solute in grain interiors, exhibiting no clear tendency to GB segregation. La, B and C were not found in chromia either as a solute impurity or at grain boundaries.

APT analysis of the oxide-alloy interface.—Since the electron microscopy analysis revealed formation of additional layers at the metal-oxide interface of three of the four studied alloys, this region was selected for a further APT analysis. Figure 8 shows combined APT atom maps for the chromia-alloy interface for the base Alloy-NbTiSi. The chemical structure around the interface appears complex, with a substantial accumulation of Nb, Si and Mn (⩾10 at% local concentrations) detected in this region. Elemental concentration profiles in Fig. 8c demonstrate that concentration peaks of these elements are spatially displaced with respect to each other, evidencing formation of a multilayer nanostructure rather than a typical segregation pattern with the coinciding spatial localization of the segregating elements. A more detailed analysis reveals formation of a discontinuous interfacial multilayer, especially for Mn and Si. The peak Mn concentration indicates possible formation of an interfacial thin $MnCr_2O_4$ spinel layer, in addition to inner spinel grains formed inside the chromia scale. Beneath the spinel-like layer, a few nm thick Si- and O-rich layer emerges with local Si concentrations up to 40 at%, indicating formation of SiO_2 phase regions. These SiO_2

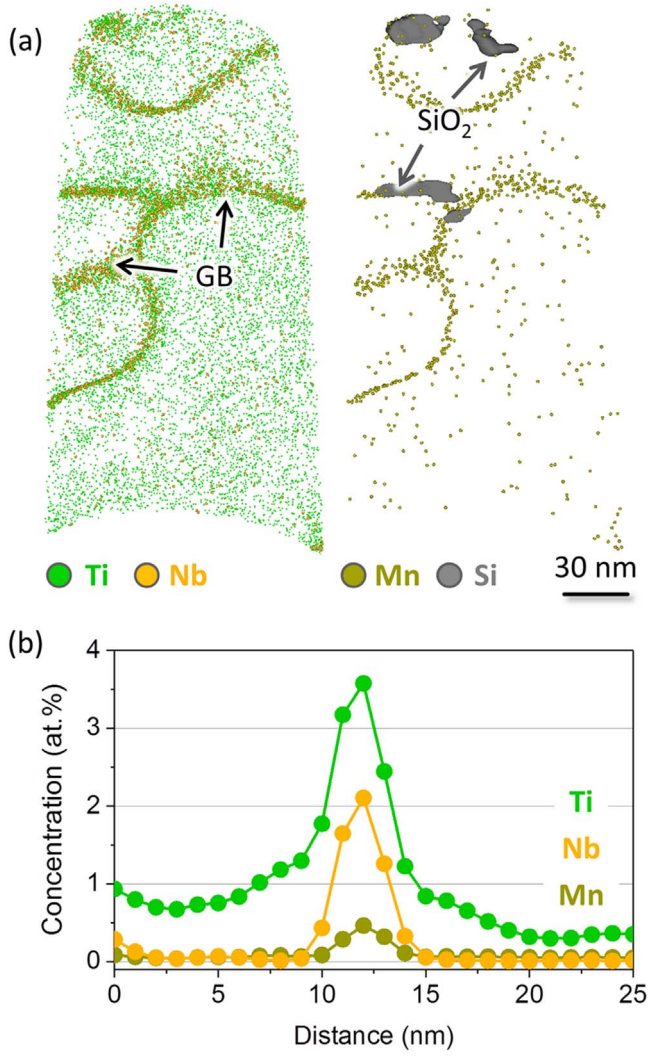

Figure 6. APT analysis of the chromia layer on Alloy-NbTi after 72 h oxidation at 800 °C in Ar-4%H_2−4%H_2O: (a) atom maps of segregating species (Ti, Nb, Si and Mn); (b) corresponding elemental concentration profiles across a GB (Si not included due to inhomogeneous segregation pattern).

regions form however not a continuous film separating the oxide scale from the alloy but rather a net-like structure with open windows, as visualized by the Si isoconcentraiton surface in Fig. 8b. Beneath the SiO_2 region, an additional thin layer of an Nb-rich oxide can be distinguished, that contains also minor additions of W and Ti. Al and La were not detected around the metal-oxide interface, while B and C were detected in negligible amounts (locally not exceeding 0.02 at%).

Unlike the base alloy, two other Nb-containing alloys (Alloy-NbTi and Alloy-Nb) form a thick continuous Nb-rich oxide between the chromia scale and the alloy. Figure 9 presents an elemental map for the interfacial region and corresponding concentration profiles across the oxide-alloy interface for Alloy-Nb (similar data for Alloy-NbTi can be found elsewhere[11]). APT reveals this oxide layer stoichiometry being close to NbO_2 rutile phase with partial substitution of Nb with Cr and, if present in the alloy, Ti. The formation of the rutile type Nb(Ti,Cr)O_2 phase in Alloy-TiNb was earlier confirmed by XRD measurements.[11] Si was found at the interface only in marginal amounts, i.e. no interfacial SiO_2 layer forms in these Si-lean alloys. Other minor alloying elements (Al and La) were not detected in the Nb(Ti,Cr)O_2 oxide or at the metal-oxide interface. An additional noticeable feature in the NbO_2-base layer is

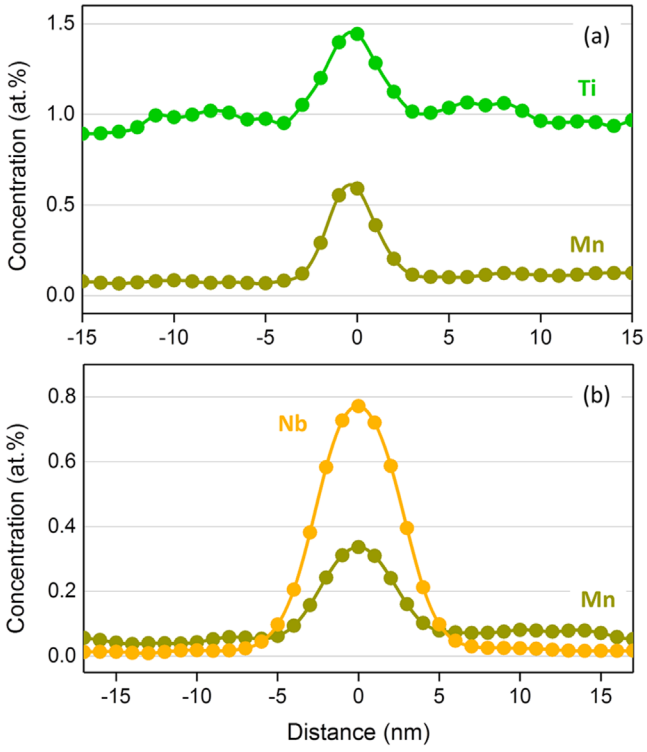

Figure 7. APT elemental concentration profiles for segregating impurities across GBs in chromia scale after 72 h oxidation at 800 °C in Ar-4%H_2−4%H_2O for (a) Alloy-Ti and (b) Alloy-Nb.

the presence of Mn enrichment at grain boundaries, with occasional appearance of inner spinel precipitates.

Compared to other alloys, Alloy-Ti (without Nb and Si) shows a direct junction of the chromia scale and the alloy matrix, as can be seen from Fig. 10. Continuous Ti segregation with a peak concentration of 2.5 at% was detected at the interface. Neither segregation of other elements nor precipitation of other phases was found at the interface or in its vicinity.

Discussion

General considerations of GB influence on the oxidation behavior.—Grain boundaries in materials, including ionic compounds and particularly oxides (e.g. bulk ceramics), provide pathways for accelerated mass transport in comparison with the conventional bulk diffusion.[48,49] Elemental segregation at GBs can substantially alter their properties, including those related to diffusion. Since the formation of the oxide scales in the current study is diffusion-controlled, apart from the transient oxidation stage, knowledge on GB segregation is important for understanding the oxidation mechanisms and especially the differences in oxidation resistance of the alloys.

Earlier studies of the oxidation behavior of high-Cr ferritic steels concluded that chromia is the first oxide scale forming on the alloy surface under high-temperature oxidation.[39] This determines the key role of chromia GBs for further oxide scale growth and the formation of the spinel layer. In particular, both inward diffusion of oxygen and outward diffusion of metal species can be strongly influenced by creating defects in the host lattice.[50] Substitution of the host ions (Cr^{3+}) at GBs with segregating ions of different charge states promotes formation of vacancies due to the necessity to maintain the charge neutrality or alter the space-charge distribution[51–53] and can eventually accelerate the mass transport. To understand the mechanism of the segregation effect, not only the types but also the amounts of segregating species need to be analyzed.

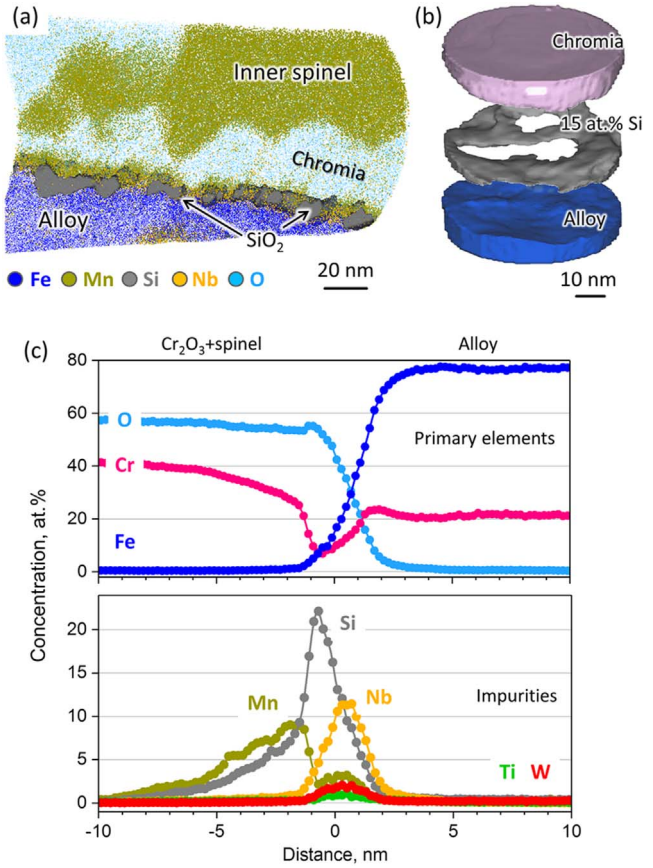

Figure 8. APT analysis of the oxide-alloy interface region in Alloy-NbTiSi (base alloy) after 72 h oxidation at 800 °C in Ar-4%H_2−4%H_2O: (a) combined atom maps for the chromia-alloy interfacial region; (b) 15 at% Si iso-concentration surface delineating the net-like SiO_2 layer forming at the metal-oxide interface; (c) proximity histograms across the interface for primary elements and impurities.

Beside the elemental segregation, the density of the grain boundary network also directly affects the mass transport, since it determines the amount of rapid diffusion paths. A denser GB network provides higher total diffusion flux and can entail faster oxidation rate in the present case of the diffusion-controlled oxidation process. The comparison of chromia grain sizes for the alloys reveals however the opposite observation (see TEM in Fig. 4): the Alloy-NbTiSi sample with smaller chromia grains (denser GB network) shows essentially slower oxidation in comparison to the larger-grained sample of the Alloy-NbTi. This indicates the dominating role of the GB segregation effect in the present study, which is discussed below.

Quantification of GB segregation from APT data.—Calculation of the Gibbsian interfacial excess G_i, i.e. the number of segregating atoms of the element *i* per GB unit area, represents a convenient and physically explicit way for quantifying and comparing GB segregation.[54] Interfacial excess values can be easily derived from APT data and, apart from that, are less affected by the data analysis artifacts as compared to other usual metrics, e.g. peak elemental concentrations at GB.[55,56]

Figure 11 summarizes the Gibbsian interfacial excess values G_i (calculated using the approach described by Maugis and Hoummada[55]) for the key elements segregating at chromia scale GBs. At least three grain boundaries were used to calculate G_i for each element in each alloy, and the average value was taken. G_i values reveal substantial variations in segregation activity of the same elements, with the most significant difference observed for Ti and Nb between Alloy-NbTiSi and the other derivative alloys.

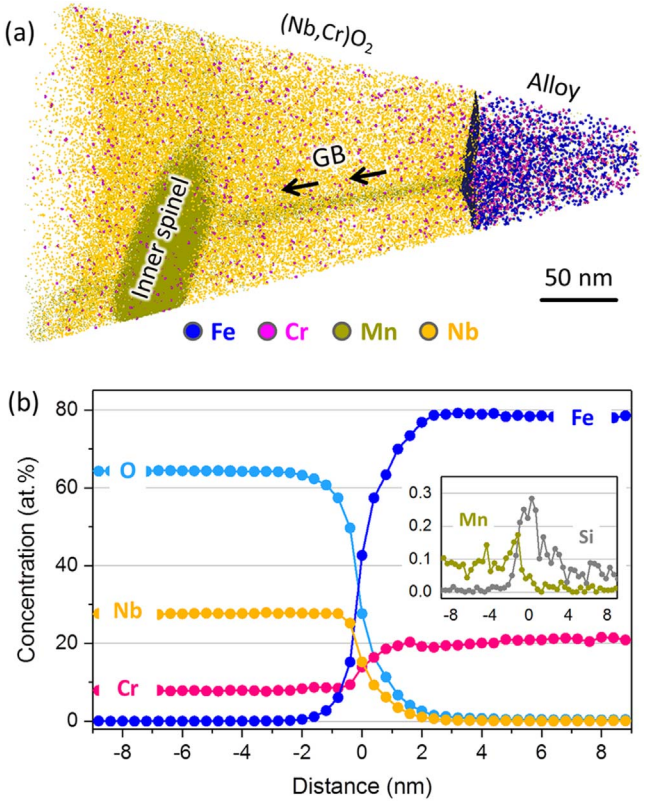

Figure 9. APT analysis of the oxide-alloy interfacial region in Alloy-Nb after 72 h oxidation at 800 °C in Ar-4%H_2−4%H_2O: (a) atom maps demonstrating formation of a (Nb,Cr)O_2 layer next to the alloy; (b) proximity histograms across the metal-oxide interface showing weak Si segregation.

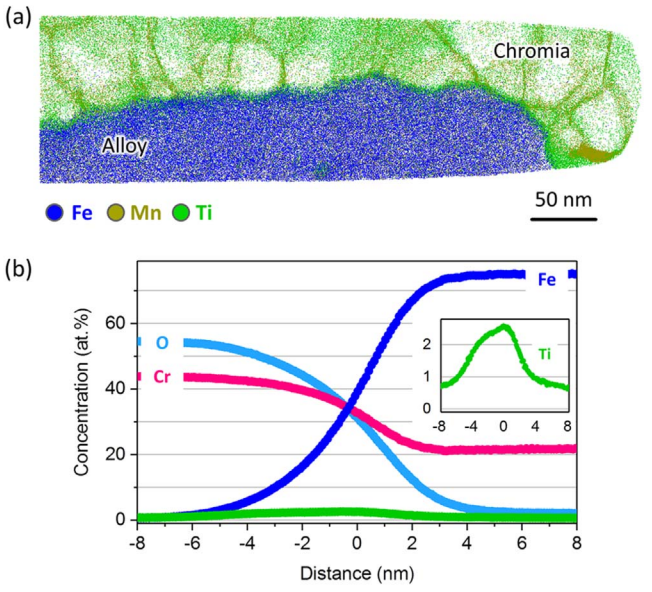

Figure 10. APT analysis of the chromia-alloy interface region in Alloy-Ti after 72 h oxidation at 800 °C in Ar-4%H_2−4%H_2O: (a) a combined atom map and (b) proximity histograms across the chromia-alloy interface. A magnified inset highlights Ti segregation at the interface.

Comparing the summary interfacial excess values with the densest cationic planes in the corundum type Cr_2O_3 phase (~10 at nm^{-2} at the (110) plane) and considering that a random GB generally has a lower cationic density, it can be concluded that the summary interfacial excess approaches or even exceeds (at least for Alloy-

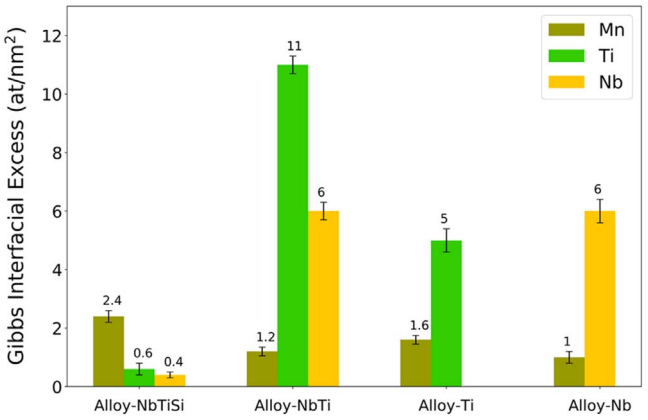

Figure 11. Gibbsian interfacial excess values G_i for grain boundary segregation of Mn, Ti and Nb in the chromia scales on the studied alloys.

NbTi) a monolayer GB coverage, which must essentially alter the microstructure and properties of the GBs.

Elemental diffusion through the chromia scale.—Our previous work concluded that Nb in the chromia scale must prevail as aliovalent Nb^{4+} or Nb^{5+} ions under the given oxidation conditions.[11] Replacement of Cr^{3+} with aliovalent Nb ions was assumed to entail formation of GB cation vacancies in order to maintain charge balance, which accelerates the outward diffusion fluxes of metallic ions, especially of Mn needed to form the top spinel layer. This mechanism can explain the high oxidation rate of Nb-containing alloys: Alloy-Nb and Alloy-NbTi indeed demonstrate high G_{Nb} values, i.e. high segregation activity of Nb. The slowly oxidizing base Alloy-NbTiSi shows an extremely low G_{Nb} at chromia GBs, probably due to the significant Nb consumption for Laves phase formation in presence of Si (visible in TEM in Fig. 4a).[7] The lowest oxidation rate of the Nb-free Alloy-Ti also aligns with the proposed mechanism.

A similar influence on the vacancy formation in chromia and eventually on the oxidation rate could be expected from titanium, once Ti ions also possess a charge state of at least 4+ in the entire oxide scale (TEM-EDS shows formation of TiO_2 precipitates underneath the metal-oxide interface). Moreover, Ti was also found within chromia grains with concentrations up to 0.8 at%, which must generate bulk vacancies via the Wagner-Hauffe doping[50] and thereby additionally contribute to the ionic mass transport through the chromia scale. Nevertheless, Alloy-Nb undergoes much faster oxidation than Alloy-Ti despite the very close G_{Nb} and G_{Ti} values, see Fig. 11. This observation indicates that the GB doping with aliovalent ions does not fully explain at least the effect of Nb.

Since GB coverage with segregating Nb and Ti reaches or even exceeds a monolayer thickness, as discussed above, one may assume formation of a thin GB layer with a local atomic environment corresponding to another phase rather than Cr_2O_3. Earlier studies demonstrated the existence of the bulk rutile-type $CrNbO_4$ phase with a wide cationic concentration range.[57] Involvement of a substantial amount of Cr into formation of a GB phase must expand its volume to two or more atomic layers, rendering alteration of the local atomic environment at GBs more plausible. The inner NbO_2-base rutile layer detected in Alloy-Nb and Alloy-NbTi shows a relatively high Cr concentration (up to 10 at%), which aligns with the wide range of Cr solubility in Nb-rich oxides. Besides, the alloys forming this additional rutile layer demonstrate high oxidation rate, indicating high permeability of the rutile phase for metallic cations. If the off-stoichiometric rutile-type local atomic environment forms at the chromia GBs, this may accelerate GB diffusion more intensively than the Wagner-Hauffe doping. To prove the viability of this mechanism, an accurate high-resolution TEM analysis of the GB regions could be helpful.

Mn forms aliovalent ions of 2+ charge state in the chromia layer, since this charge state is characteristic for the topmost $MnCr_2O_4$ spinel with the highest pO_2 level, i.e. with the highest possible charge state in the oxide scale. In terms of GB vacancy formation, this should counterweight the effect of Nb and Ti. The most notable here is the base Alloy-NbTiSi, where Mn segregation at GBs exceeds that of Ti and Nb together ($G_{Mn} > G_{Ti} + G_{Nb}$), which should reverse the charge balance at GBs toward positive charge deficiency. This can be mitigated by partial removal of negative charge, i.e. by creation of oxygen vacancies, promoting inward oxygen transport instead of outward cation diffusion. This mechanism may explain the small thickness of the outer spinel layer in Alloy-NbTiSi (due to slow outward Mn diffusion) as well as appearance of small chromia grains in the vicinity of the metal-oxide interface (fast O diffusion promotes inner nucleation of Cr_2O_3), which are distinguishable in TEM and even in APT by the GB segregation pattern (Fig. 8a). Slow Mn diffusion may be also responsible for the extensive formation of the inner spinel grains in Alloy-NbTiSi due to accumulation of Mn at grain boundaries (the highest G_{Mn} value among all alloys) with further nucleation and growth of the $MnCr_2O_4$ phase in the inner region of the chromia.

Intermittent oxide phases between chromia and alloy.—Two of the studied Nb-containing alloys, Alloy-Nb and Alloy-NbTi, form an intermittent Nb-rich oxide layer of 100–200 nm thickness, with a composition matching $Nb(Ti,Cr)O_2$ rutile (see Fig. 9b). As mentioned above, this phase does apparently not limit the cation diffusion through the oxide scale, since these alloys show high oxidation rates. APT was helpful to reveal the diffusion pathways of the main oxide formers, Cr and Mn, through this rutile layer. Namely, Mn can diffuse through rutile GBs, since APT evidences Mn presence along them. Cr can diffuse along GBs as well and additionally through its bulk, as Cr solubility in the rutile up to 9 at. % was observed. Alloy-NbTiSi also forms a thin Nb-rich oxide layer, as indicated by the Nb concentration peak at the metal-oxide interface (Fig. 8c), but high Nb consumption by the Laves phase limits its thickness to only a few nm.

Analysis of the interfacial region in Alloy-NbTiSi reveals also the formation of an additional Si-rich oxide layer. A continuous SiO_2 layer at the metal-oxide interface is considered to be strongly detrimental for the interconnect performance in an SOFC/SOEC due to its high electrical resistivity.[8] TEM-EDS analysis indeed shows an apparently continuous Si-rich oxide at the interface. APT analysis confirms the SiO_2 stoichiometry of these Si-rich regions but reveals its net-like morphology with only partial interface coverage (see Fig. 8b). Open windows in the SiO_2 layer should provide the necessary electrical conductivity after oxidation, thus not preventing an interconnect plate made of this alloy to act as a current collector in fuel/electrolysis cell devices. Although the interfacial coverage with SiO_2 is quite high after 72 h oxidation, further SiO_2 formation is apparently hindered or even prevented due to active Si consumption by the forming Laves phase, and no continuous silica subscale emerges, since this alloy demonstrates a good long-term SOFC/SOEC performance.[10]

Reactive element effect.—An additional comment should be given to the role of La as a reactive element. Earlier studies concluded that it has a positive influence on oxide scale adherence or oxidation rate on many high-Cr steels.[38] The assumed explanations for the reactive element effect were (1) its segregation in the oxide scale with a direct influence on the growth process, (2) its segregation at the metal-oxide interface and thereby direct alteration of the adhesion properties and (3) binding detrimental impurities, first of all sulphur, inside the cast alloy. La was added to three of the studied alloys in order to directly check the first two assumptions by APT. Possible peaks of La or LaO_x ions of different charge states in the mass spectra do not overlap with other ions, so La detection by APT was expected to be easy. Nevertheless, no La was found by APT in any part of the oxide scale, at the metal-oxide interface or in

the alloy matrix directly beneath the interface for all alloys (see the Supplementary Information for more detail). This observation seems to rule out the mentioned mechanisms (1) and (2) for the studied alloys, which imply a direct involvement of La in the oxidation process.

Conclusions

Four high-Cr ferritic steels with a nominal base composition Fe-22Cr-0.4Mn (wt%) and various contents of minor Nb, Ti and Si additions were oxidized in a model Ar-4%H_2−4%H_2O atmosphere at 800 °C. All studied materials showed formation of a duplex oxide scale consisting of $MnCr_2O_4$ spinel forming on top of Cr_2O_3. A thermogravimetric analysis of oxidation kinetics indicated that, after the transient oxidation, the scale growth was controlled by diffusion processes within the oxide. A detailed APT analysis of the key regions influencing the diffusion through the oxide scale (chromia and metal-oxide interface) revealed the determining role of GB segregation in the oxidation processes, and established relationships between the composition, the microstructure and oxidation behavior.

The main conclusions can be formulated as follows:

1) Mn, Ti and Nb actively segregate at chromia GBs. Gibbsian interfacial excess G_i values indicate a monolayer or higher GB coverage with Nb + Ti in alloys with low Si content. Substitution of the host Cr^{3+} ions with higher-charged Nb^{4+}/Nb^{5+} and Ti^{4+} ions (Wagner-Hauffe doping) can promote formation of cationic vacancies, thereby accelerating outward cation diffusion along GBs and eventually increasing the oxidation rate. Nevertheless, the vacancy formation mechanism cannot solely explain the much stronger effect of Nb compared to that of Ti, indicating a possible alteration of GB structure in presence of Nb with further changes in GB diffusion properties.
2) Nb-containing alloys with low Si concentration exhibit an additional rutile-type Nb(Cr,Ti)O_2 layer between chromia and metal matrix. This layer does not inhibit outward diffusion of Mn (proceeding through GBs) and Cr (proceeding through GB and/or bulk) necessary to form the main chromia/spinel scale. Addition of Si promotes Laves phase formation within the steel, which actively binds Nb and prevents it from entering the oxide scale, thereby providing a low oxidation rate for the base Alloy-NbTiSi.
3) GB segregation of lower charged Mn^{2+} ions apparently mitigates the effect of Nb and Ti. Alloys showing at chromia GBs a relatively high Gibbs interfacial excess of Mn (G_{Mn}) in comparison to G_{Nb} + G_{Ti} (Alloy-Ti and Alloy-NbTiSi) exhibit slower oxidation, which may be explained by lower concentration of cation vacancies and even the counter-formation of oxygen vacancies promoting inward O diffusion. This results in slow growth of the outermost spinel layer and formation of inner spinel grains (due to slow outward Mn diffusion) in Alloy-NbTiSi.
4) La (reactive element) was not detected by APT in the oxide scale as well as around the metal-oxide interface for all La-containing alloys, indicating no direct influence of La on the oxide scale formation.

Acknowledgments

One of the authors (A.V.) is grateful for the HiTEC Graduate school of Forschungszentrum Jülich GmbH, Germany for providing financial support for his PhD stay. The authors acknowledge their colleagues Dr. Egbert Wessel (SEM and TEM) and Heiko Cosler (thermogravimetry) from the Institute of Microstructure and Properties of Materials (IEK-2), Forschungszentrum Jülich GmbH for assistance with the measurements.

ORCID

Ivan Povstugar https://orcid.org/0000-0002-1409-6854

References

1. N. Minh, J. Mizusaki, and S. C. Singhal, *ECS Trans.*, **78**, 63 (2017).
2. S. R. Foit, I. C. Vinke, L. G. J. de Haart, and R. A. Eichel, *Angew. Chemie Int. Ed*, **56**, 5402 (2017).
3. Q. Fu, C. Mabilat, M. Zahid, A. Brisse, and L. Gautier, *Energy Environ. Sci.*, **3**, 1382 (2010).
4. Z. Gao, L. V. Mogni, E. C. Miller, J. G. Railsback, and S. A. Barnett, *Energy Environ. Sci.*, **9**, 1602 (2016).
5. J. Zurek, N. Margaritis, D. Naumenko, N. H. Menzler, and W. J. Quadakkers, *Oxid. Met.*, **92**, 353 (2019).
6. B. Kuhn, C. A. Jimenez, L. Niewolak, T. Hüttel, T. Beck, H. Hattendorf, L. Singheiser, and W. J. Quadakkers, *Mater. Sci. Eng. A*, **528**, 5888 (2011).
7. J. Froitzheim, G. H. Meier, L. Niewolak, P. J. Ennis, H. Hattendorf, L. Singheiser, and W. J. Quadakkers, *J. Power Sources*, **178**, 163 (2008).
8. L. Niewolak, F. Tietz, and W. J. Quadakkers, *High-Temperature Solid Oxide Fuel Cells for the 21st Century* (Elsevier, Amsterdam) p. 195 (2016).
9. H. Asteman, J. E. Svensson, L. G. Johansson, and M. Norell, *Oxid. Met.*, **52**, 95 (1999).
10. L. Niewolak, D. J. Young, H. Hattendorf, L. Singheiser, and W. J. Quadakkers, *Oxid. Met.*, **82**, 123 (2014).
11. A. Vayyala, I. Povstugar, T. Galiullin, D. Naumenko, W. J. Quadakkers, H. Hattendorf, and J. Mayer, *Oxid. Met.*, **92**, 471 (2019).
12. P. Huczkowski, *Thesis* (2005), Techn. HochschAachen http://juser.fz-juelich.de/record/48666.
13. W. J. Quadakkers, J. Pirón-Abellán, and V. Shemet, *Mater. Res.*, **7**, 203 (2004).
14. P. Huczkowski, V. Shemet, J. Piron-Abellan, L. Singheiser, W. J. Quadakkers, and N. Christiansen, *Mater. Corros.*, **55**, 825 (2004).
15. M. P. Brady, B. A. Pint, Z. G. Lu, J. H. Zhu, C. E. Milliken, E. D. Kreidler, L. Miller, T. R. Armstrong, and L. R. Walker, *Oxid. Met.*, **65**, 237 (2006).
16. L. Niewolak, L. Blum, R. Peters, D. Grüner, and W. J. Quadakkers, *Fuel Cells*, **16**, 600 (2016).
17. L. Garcia-Fresnillo, L. Niewolak, W. J. Quadakkers, and G. H. Meier, *Oxid. Met.*, **89**, 61 (2018).
18. A. Gil, O. Kryshtal, T. Brylewski, and A. Czyrska-Filemonowicz, *Surf. Coatings Technol.*, **368**, 232 (2019).
19. H. Falk-Windisch, P. Malmberg, M. Sattari, J. E. Svensson, and J. Froitzheim, *Mater. Charact.*, **136**, 128 (2018).
20. C. M. Cotell, G. J. Yurek, R. J. Hussey, D. F. Mitchell, and M. J. Graham, *Oxid. Met.*, **34**, 201 (1990).
21. D. Clemens, V. Vosberg, W. Hobbs, U. Breuer, W. J. Quadakkers, and H. Nickel, *Anal. Bioanal. Chem.*, **355**, 703 (1996).
22. S. B. Newcomb, D. J. Smith, and W. M. Stobbs, *J. Microsc.*, **130**, 137 (1983).
23. J. H. Kim, B. K. Kim, D. I. Kim, P. P. Choi, D. Raabe, and K. W. Yi, *Corros. Sci.*, **96**, 52 (2015).
24. I. Povstugar, J. Weber, D. Naumenko, T. Huang, M. Klinkenberg, and W. J. Quadakkers, *Microsc. Microanal.*, **25**, 11 (2019).
25. K. Stiller, L. Viskari, G. Sundell, F. Liu, M. Thuvander, H. O. Andrén, D. J. Larson, T. Prosa, and D. Reinhard, *Oxid. Met.*, **79**, 227 (2013).
26. T. D. Nguyen, A. La Fontaine, L. Yang, J. M. Cairney, J. Zhang, and D. J. Young, *Corros. Sci.*, **132**, 125 (2018).
27. A. La Fontaine, H. W. Yen, P. J. Felfer, S. P. Ringer, and J. M. Cairney, *Scr. Mater.*, **99**, 1 (2015).
28. P. Kontis, S. Pedrazzini, Y. Gong, P. A. J. Bagot, M. P. Moody, and R. C. Reed, *Scr. Mater.*, **127**, 156 (2017).
29. K. A. Unocic, Y. Chen, D. Shin, B. A. Pint, and E. A. Marquis, *Micron*, **109**, 41 (2018).
30. S. Pedrazzini, D. J. Child, G. West, S. S. Doak, M. C. Hardy, M. P. Moody, and P. A. J. Bagot, *Scr. Mater.*, **113**, 51 (2016).
31. Y. Chen, R. C. Reed, and E. A. Marquis, *Oxid. Met.*, **82**, 457 (2014).
32. T. Boll, K. A. Unocic, B. A. Pint, and K. Stiller, *Microsc. Microanal.*, **23**, 396 (2017).
33. G. Sundell, M. Thuvander, and H.-O. Andrén, *Corros. Sci.*, **65**, 10 (2012).
34. R. Steinberger-Wilckens, L. Blum, H. P. Buchkremer, B. De Haart, J. Malzbender, and M. Pap, *ECS Trans.*, **35**, 53 (2011).
35. H. Nabielek et al., *Advances in Solid Oxide Fuel Cells III* (John Wiley & Sons, New York) p. 65 (2009).
36. L. Blum et al., *Fuel Cells*, **7**, 204 (2007).
37. L. Blum, H.-P. Buchkremer, S. M. Gross, B. de Haart, J. W. Quadakkers, U. Reisgen, R. Steinberger-Wilckens, R. W. Steinbrech, and F. Tietz, *ECS Proc*, **2005–07**, 39 (2005).
38. J. Quadakkers and L. Singheiser, *Mater. Sci. Forum*, **369–372**, 77 (2001).
39. W. J. Quadakkers, J. Piron-Abellan, V. Shemet, and L. Singheiser, *Mater. High Temp.*, **20**, 115 (2003).
40. R. P. Oleksak, M. Kapoor, D. E. Perea, G. R. Holcomb, and Ö. N. Doğan, *npj Mater. Degrad.*, **2**, 25 (2018).
41. S. C. Singhal and K. Kendall, *High Temperature and Solid Oxide Fuel Cells* (Elsevier, Amsterdam) p. 406 (2003).
42. K. Thompson, D. Lawrence, D. J. Larson, J. D. Olson, T. F. Kelly, and B. Gorman, *Ultramicroscopy*, **107**, 131 (2007).
43. W. J. Quadakkers, D. Naumenko, E. Wessel, V. Kochubey, and L. Singheiser, *Oxid. Met.*, **61**, 17 (2004).

44. B. A. Pint and K. L. More, *J. Mater. Sci.*, **44**, 1676 (2009).
45. O. C. Hellman, J. A. Vandenbroucke, J. Rüsing, D. Isheim, and D. N. Seidman, *Microsc. Microanal.*, **6**, 437 (2000).
46. M. Karahka, Y. Xia, and H. J. Kreuzer, *Appl. Phys. Lett.*, **107**, 062105 (2015).
47. A. Devaraj, R. Colby, W. P. Hess, D. E. Perea, and S. Thevuthasan, *J. Phys. Chem. Lett.*, **4**, 993 (2013).
48. W. D. Kingery, H. K. Bowen, and D. R. Uhlmann, *Introduction to Ceramics* (John Wiley & Sons, New York) 2nd ed., p. 1056 (1976).
49. D. J. Young, *High Temperature Oxidation and Corrosion of Metals* (Elsevier, Amsterdam) p. 758 (2016).
50. P. Kofstad, *High Temperature Oxidation of Metals* (John Wiley & Sons, New York) p. 354 (1966).
51. K. L. Kliewer and J. S. Koehler, *Phys. Rev.*, **140**, A1226 (1965).
52. M. F. Van, R. M. Cannon, H. K. Bowen, and R. L. Coble, *J. Am. Ceram. Soc.*, **60**, 120 (1977).
53. W. Kingery, *Solid State Ionics*, **12**, 299 (1984).
54. B. W. Krakauer and D. N. Seidman, *Phys. Rev. B*, **48**, 6724 (1993).
55. P. Maugis and K. Hoummada, *Scr. Mater.*, **120**, 90 (2016).
56. O. C. Hellman and D. N. Seidman, *Mater. Sci. Eng. A*, **327**, 24 (2002).
57. C. J. Chen, M. Greenblatt, K. R. Nair, and J. V. Waszczak, *J. Solid State Chem.*, **64**, 81 (1986).